Article

A Synergic Application of High-Oxygenated E-Fuels and New Bowl Designs for Low Soot Emissions: An Optical Analysis

José V. Pastor [1], Carlos Micó [1,*], Felipe Lewiski [1], Francisco J. Tejada [1] and Cinzia Tornatore [2]

1. CMT—Motores Térmicos, Universitat Politècnica de València, Camino de Vera s/n, 46022 Valencia, Spain; jpastor@mot.upv.es (J.V.P.); fedevar@mot.upv.es (F.L.); fratemag@mot.upv.es (F.J.T.)
2. Istituto di Scienze e Tecnologie per l'Energia e La Mobilità Sostenibili (STEMS-CNR), Via Marconi 4, 80125 Naples, Italy; cinzia.tornatore@stems.cnr.it
* Correspondence: carmirec@mot.upv.es; Tel.: +34-65-491-9619

Abstract: Synthetic fuels significantly reduce pollutant emissions and the carbon footprint of ICE applications. Among these fuels, oxymethylene dimethyl ethers (OME_X) are an excellent candidate to entirely or partially replace conventional fuels in compression ignition (CI) engines due to their attractive properties. The very low soot particle formation tendency allows the decoupling of the soot-NO_X trade-off in CI engines. In addition, innovative piston geometries have the potential to reduce soot formation inside the cylinder in the late combustion stage. This work aims to analyze the potential of combining OME_X with an innovative piston geometry to reduce soot formation inside the cylinder. In this way, several blends of OME_X-Diesel were tested using a radial-lips bowl geometry and a conventional reentrant bowl. Tests were conducted in an optically accessible engine under simulated EGR conditions, reducing the in-cylinder oxygen content. For this purpose, 2-colour pyrometry and high-speed excited state hydroxyl chemiluminescence techniques were applied to trace the in-cylinder soot formation and oxidation processes. The results confirm that increasing OME_X in Diesel improves the in-cylinder soot reduction under low oxygen conditions for both piston geometries. Moreover, using radial lips bowl geometry significantly improves the soot reduction, from 17% using neat Diesel to 70% less at the highest OME_X quantity studied in this paper.

Keywords: E-fuels; soot reduction; radial lips; piston geometry; emission reduction

1. Introduction

The tight pollution regulation and ongoing rise in energy consumption have pushed the car industry to look for new and more effective internal combustion engine technologies to achieve the zero pollution target. It sets out the vision that by 2050, the European Union (EU) should have reduced pollution to the extent that it no longer harms human health and natural ecosystems. This vision is translated into crucial 2030 targets to reduce pollution at source. Although the transport sector has made good progress toward reducing harmful emissions, further efforts will be needed to eliminate all its negative impacts [1]. However, this sector has difficulties reducing the soot-NO_X trade-off and achieving a neutral carbon footprint in compression ignition (CI) engines [2].

Using renewable, low carbon non-fossil based fuels for ICE applications is a promising option to reduce pollutant emissions and carbon footprint [3,4]. Several studies showed the potential of these fuels to achieve emission reduction objectives in different facilities, such as engines [5–8] and optical vessels [9,10]. Among these fuels, oxymethylene dimethyl ethers (OME_n) are attractive due to their physicochemical properties [11]. Their molecular structure is $CH_3-O-(CH_2-O)_n-CH_3$, where n explicitly the chain length ($n = 1–6$) directly affects the physicochemical properties of the fuel. The lack of C-C bonds and the presence of oxygen have shown a high potential of these fuels to reduce or even avoid soot formation inside the combustion chamber [12]. These fuels are usually presented as a blend of OME_n

molecules (known as OME_X), which allows for achieving more similar properties to those of conventional Diesel than using only OME_n single-component molecules. In addition to their molecular structure characteristics, properties such as a high cetane number compared to Diesel improve autoignition performance. For these reasons, OME_X is a good candidate to replace fossil fuels in ICE [13].

However, using neat OME_X as a fuel in ICE still needs to face several challenges related to compatibility with the engine infrastructure, such as filters and other fuel system parts [14] due to their low lubricity and swelling corrosion effect on rubber and plastics. To overcome this limitation, OME_X blended with conventional Diesel has also been proposed in several studies, reporting that these blends can avoid the infrastructure problem while still offering the benefits of OME_X in terms of soot reduction [15]. García et al. [16] reported decreased unburned hydrocarbons (HC) at the engine exhaust using these blends. However, other authors reported slightly higher NO_X emissions [17]. For this reason, strategies to reduce the combustion chamber temperature, and thus NO_X formation, are mandatory. In this way, the use of exhaust gas recirculation (EGR) schemes are typically used in CI [18] and spark ignition (SI) [19] engines. However, these strategies, based on reducing the oxygen content inside the combustion chamber by adding burnt gases from the exhaust, promote soot particle formation and an increase of HC emissions [20], showing the existing soot-NO_X trade-off.

Another option to reduce pollutant emissions in ICE applications is using innovative hardware designs [21,22]. In this regard, significant focus has been placed on studying new piston geometries for CI engines, with many designs created and tested over the previous years. The aim has been to modify the turbulent flow structure in-cylinder air-fuel mixing, soot production, and thermal efficiency [23]. One proposal is redirecting the flames toward the piston center using innovative bowl geometries. The aim is to use available oxygen in this zone to oxidize the soot. In addition, this geometry could reduce (or avoid) the direct flame-to-flame interaction [24]. In this way, the reentrant bowl design allows the flames to be redirected towards the piston center after wall impingement, being fed with the oxygen still available in this region during the late stages of the combustion process. This increases late soot oxidation [25]. An evolution of this piston design includes a stepped lip at the upper part of the reentrant bowl to split the sprays, driving some fuel toward the squish region and taking advantage of the oxygen usage there [26,27]. The most recent modification of the piston geometry includes protrusions at the piston periphery. Volvo Group initially presented the design of these protrusions for heavy-duty engines [25,28]. Studies reported an improvement in soot reduction and efficiency compared to the previous piston designs [24]. However, an increase in HC emissions has also been reported using this geometry [29], mainly at higher loads. This effect has been related to promoting lean mixture regions and spray impingement on the piston and liner surface.

Considering all the above, there is a literature gap related to the study of possible synergies between these two approaches (oxygenated fuels and improved piston geometries) to reach low-soot combustions. Therefore, the current study aims to evaluate the potential of using oxygenated fuels, like OME_X, in combination with novel bowl designs, like radial lips, to reduce in-cylinder soot formation.

For this purpose, several blends of OME_X and Diesel (0%, 30%, and 50% of OME_X) have been tested combined with a radial-lips bowl piston and a reentrant bowl piston. In addition, the reduction of oxygen content inside the combustion chamber (15% O_2) was evaluated to simulate EGR conditions, typically to reduce NO_X formation. The work applied 2-colour pyrometry and high-speed excited state hydroxyl (OH*) techniques in an optical single-cylinder CI engine to trace the soot formation and oxidation processes. The main result shows that at low in-cylinder oxygen conditions, the radial-lips piston combined with the OME_X blend significantly improves the soot reduction inside the combustion chamber for the whole event. Moreover, this effect is more noticeable with the increase of OME_X.

2. Experimental Methodology

2.1. Optical Engine Facility

The tests were carried out in a Bowditch optical engine design, as can be seen in Figure 1, based on a medium-duty CI platform. This engine has the typical overhead valve design, where the camshaft is located at the engine block and connected to the crankshaft via a gear. Push rods are used for opening and closing the valves. In this facility, a specific box was installed just on the cylinder side to allocate the camshaft, as the distance between the head and block is increased due to the optical access design. Due to this adaptation, there are no lateral optical accesses to the combustion chamber, allowing just the visualization through the piston bottom. The optical engine uses the same original cylinder head as the conventional version. It has four valves and a centered solenoid injector per cylinder. In Table 1, the main geometric parameters of the optical engine are summarized.
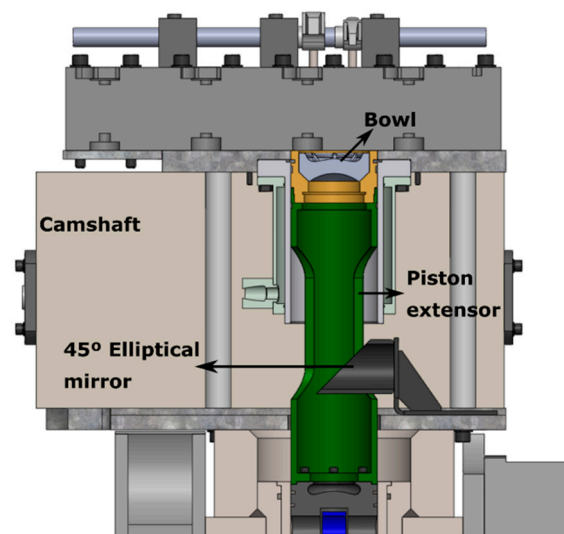

Figure 1. Optical engine parts. Reprinted with permission [24].

Table 1. Optical engine characteristics.

Parameter	Value
Number of cylinders [-]	1
Number of valves [-]	4
Compression ratio	13.3
Stroke/Bore	~1
Displacement [L]	~0.8

The fuel was delivered to the injector using a high-pressure pump (Bosch CP3, Gerlingen, Germany) and a conventional common rail. A Controlled Diffusive Spray (CDS) injector with eight holes was employed for the current work. This injector allows an improving the distribution of the spray inside the chamber. The result is a shorter penetration of the spray and a wider cone angle. The result is a closer combustion reaction to the center of the piston bowl, as opposed to the traditional nozzles, that the combustion reactions appear close to the walls [30]. Several numerical [31] and experimental [23,32,33] studies have shown a significant reduction in pollutant emissions, particularly in particulate matter and hydrocarbon emissions. Thermodynamic analysis was performed thanks to a fully instrumented engine. The instantaneous intake and exhaust pressures were measured using a piezoresistive transducer (Kistler 4049A5 Switzerland). A piezoelectric transducer (Kistler 6124A, Switzerland) was used for registering the in-cylinder pressure. The pressure signals were synchronized with a crankshaft encoder with a 0.5 crank angle degree (CAD) resolution. In addition, intake and exhaust temperatures and oil and coolant temperatures

were measured with K-type thermocouples. The first thermodynamic law calculates the apparent heat release rate (aRoHR). A screw compressor provides the intake air at the required pressure, and a valve at the exhaust system simulates the back pressure of 0.2 bar. An air heater was located just before the intake port to set the intake air temperature required for each test. The engine was run in skip-fire mode to reduce thermal stress, window fouling, and thermal transients [34]. As a result, just one combustion cycle occurred each 20 motored cycles.

2.2. Piston Geometries

Figure 2 presents the two bowl designs employed in this investigation: a conventional piston (left side) and a radial-lips piston (right side). The conventional piston, commonly used in light and medium-duty engines, shows a typical reentrant bowl geometry. The radial-lips piston combines two features: a stepped lip at the bowl top edge and radial lips distributed around the bowl circumference. The stepped lip is expected to promote combustion at the squish zone, while the radial lips improve oxygen utilization in the bowl center. In addition, they reduce the flame-to-flame interaction at the periphery. The two pistons provide the same compression ratio, guaranteeing the same in-cylinder ambient conditions, allowing a direct comparison between them.
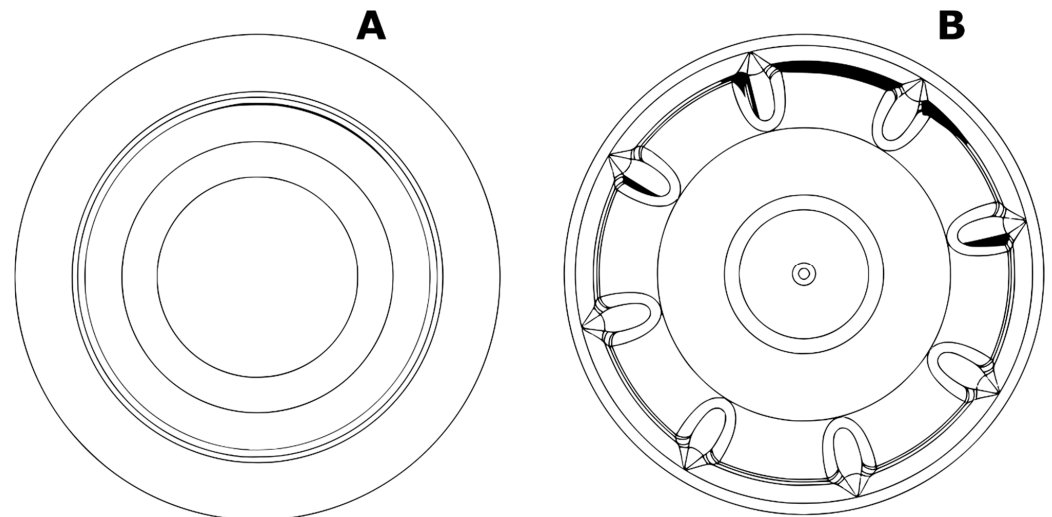

Figure 2. (**A**) Conventional piston and (**B**) Radial-lips piston.

2.3. Optical Techniques and Methodology

This study used 2-color pyrometry (2C) and OH* high-speed imaging to analyze the evolution of soot formation and oxidation processes in the combustion chamber. The optical setup is shown in Figure 3. The flame radiation from the combustion chamber passes through the quartz piston, and the 45° elliptical mirror reflects it. This mirror has an enhanced aluminium coating to obtain a good reflection efficiency in the ultraviolet (UV) and visible spectra (above 85% between 250 nm and 700 nm). Then, using a dichroic mirror (DMSP805L), the incident radiation is split: visible light is transmitted while a small range of UV spectrum, around 310 nm, is reflected. A high-speed intensified camera with a narrowband interference filter detects the reflected UV radiation. In addition, the transmitted visible light goes to a beam splitter, reflecting 50% and transmitting the other 50% of the total incident light. Both radiations are collected using two high-speed cameras equipped with specific bandpass filters to detect the light at a particular wavelength for applying the 2-color pyrometry algorithm. The same start of energizing (SOE) electric pulse used for the injector serves as a trigger for all the cameras. Thus, time-synchronized images from all cameras are obtained. This allows a direct comparison between the frames of each camera, which is critical for the 2C technique.
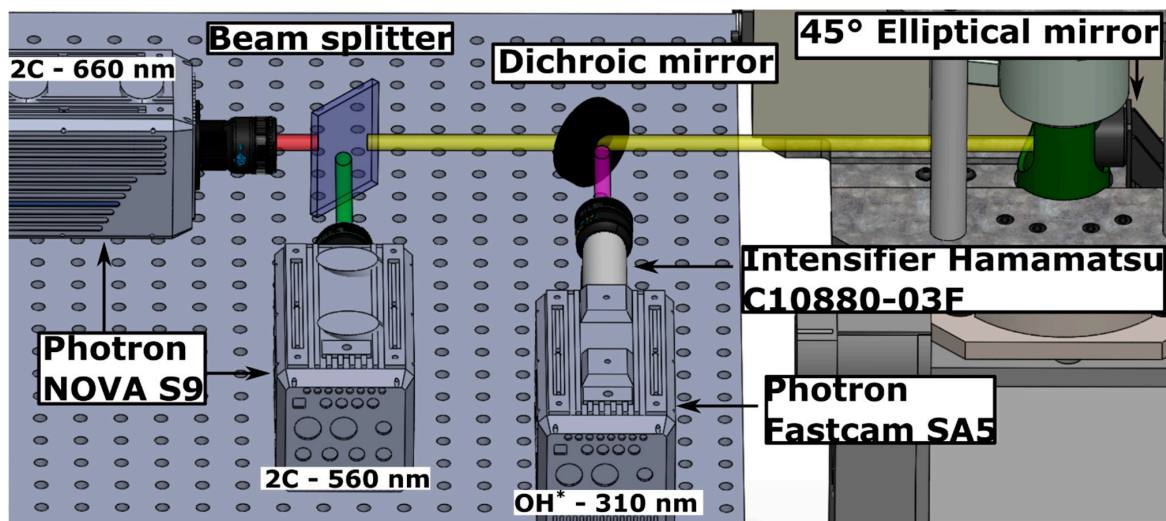
Figure 3. A sketch of the optical setup used to apply both OH* chemiluminescence and 2-color pyrometry techniques.

2.3.1. OH* Chemiluminescence Radiation

The OH* chemiluminescence radiation is an excellent high-temperature reaction tracer in diffusive flames [35,36]. Thus, high-speed OH* chemiluminescence was performed to trace the oxidation reactions inside the combustion chamber during the combustion process in this study. It is essential to consider that this is a line-of-sight integrated technique.

The optical setup (Figure 3) is composed of a high-speed CMOS camera (Photron SA5) coupled with a high-speed intensifier (Hamamatsu C10880-03F) with 1:1 relay optics. The intensifier photocathode is a multi-alkali (S-20), which allows detection from UV to near-infrared radiation (spectral response: 185–900 nm). A UV-Nikor Rayfact lens with a focal length of 105 mm and a maximum f-aperture of 4.5 is used. To collect the OH* peak emission, a narrowband interference filter centered at 310 nm with a full width at half maximum (FWHM) of 10 nm was used in front of the camera lens. Using this filter helps to avoid other radiation sources that can interfere with the OH* signal. The acquisition rate was set at 25 kfps with a resolution of 4.4 pixels/mm. The same exposure time used in the high-speed camera, which is 39.75 μs, was set in the gating of the intensifier. In addition, the intensifier gain was fixed to 900 (ranging from 600 to 999).

2.3.2. 2-Color Pyrometry Technique

The in-cylinder soot concentration evolution (KL factor) can be analyzed using the 2-Color pyrometry technique by collecting the soot thermal radiation at two different wavelengths. More details about the method and the radiation analysis can be found in [37].

The setup comprises two identical high-speed cameras (Photron NOVA S9) with different bandpass filters (see Figure 3). One of the cameras is equipped with a filter centered at 660 nm, while the other is centered at 560 nm. Both filters have a 10 nm FWHM. Most of the dynamic range of both cameras was ensured by adjusting the exposure time of them, depending on the operating condition: 0.5 μs (660 nm camera) and 5 μs (560 nm camera) at 21% O_2, and 0.7 μs (660 nm camera) and 20 μs (560 nm camera) at 15% O_2. Furthermore, both cameras were coupled with a Karl-Zeiss Makroplanar lens with a 100 mm focal length and a maximum f-aperture of 2. The frame rate was fixed at 25 kfps, corresponding to the same frame rate used for the OH* chemiluminescence imaging, with a resolution of 4.6 pixels/mm.

For accurate implementation of the 2C algorithm, it is essential to ensure temporal and spatial matching between the signal of two wavelengths. As mentioned earlier, temporal matching is achieved by synchronizing the acquisition of both cameras. Regarding spatial

alignment, it can be accomplished by employing a preprocessing routine that utilizes the reference wavelength to transform the signal at the other wavelength. This routine involves a transformation matrix encompassing translation, rotation, and scaling. Applying a scale-invariant method [38], a set of feature points is extracted from the images of both wavelengths. Subsequently, the matching between the feature points from both lists is calculated to derive the spatial transformation matrix. Finally, this transformation matrix is applied to one of the wavelengths to achieve spatial alignment. It is important to note that the spatial matrix transformation is computed for each iteration.

Once the transformation matrix has been applied, the 2C algorithm obtains the spatial distribution of KL inside the combustion chamber. It is calculated for each repetition and averaged pixel by pixel (10 repetitions) to avoid the combustion stochastic behavior hindering the analysis. This procedure is applied for the whole combustion event to obtain the temporal evolution of the spatial KL distribution inside the combustion chamber. Furthermore, average time evolution curves are obtained by calculating the ensemble average of KL along the whole field of view. A circular mask (a matrix composed of ones and zeros) is applied to the raw images to consider only the radiation inside the combustion chamber and reject radiation from outside (see Figure 4). The KL distributions reported in this paper are represented using the same intensity range and a 16-color Look Up Table.
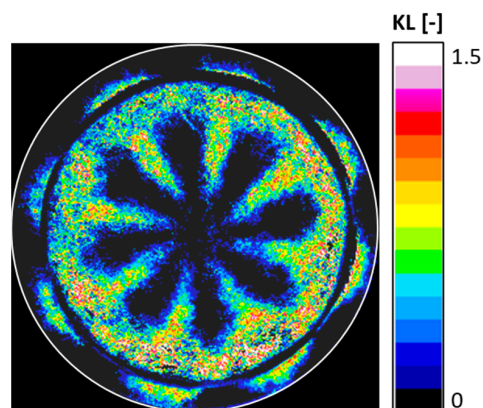

Figure 4. Typical KL distribution. The white circle indicates the area considered for calculating the ensemble average KL.

2.3.3. Post-Processing: Evolution Maps

A procedure has been followed to represent the evolution of KL values and OH* spatial distribution inside the combustion chamber during the whole combustion process in a single map. It divides the combustion chamber into concentrical rings, for which the average KL or OH* intensity value is calculated. This way, an average intensity value is obtained for different radii from the center of the piston. This procedure is carried out for each frame, corresponding to a different CAD. The result is a 2D matrix where each column represents a different CAD while the row is the radial distance to the center of the piston. An example of the result from this methodology is illustrated in Figure 5. The green and red lines indicate the minimum and maximum radial distances shown on the map, respectively. In this study, the analysis does not consider the squish zone (the area between red and white lines in the left image). The average KL values of the different rings at a specific CAD are represented between the two white lines in the right image. The value of a particular ring, represented in purple in the left image, has been highlighted with the same color in the 2D map. The same methodology is followed for OH* chemiluminescence.

2.4. Operating Conditions

All the tests were performed at a fixed engine speed of 1400 rpm, reaching 6 bar of brake mean effective pressure (BMEP). For each piston geometry, three fuels were investigated: pure Diesel (0 Ox), a blend of 70% Diesel and 30% OME$_X$ by mass (30 Ox),

and a mixture of 50% Diesel and 50% OME$_X$ by mass (50 Ox). The different percentages used in this study have shown good miscibility in previous studies [16]. Two different oxygen concentrations in the combustion chamber were tested for each fuel: 21% and 15%. The 15% of oxygen simulated the optical engine operating under EGR conditions. A total of 12 different operating points were investigated. The operating conditions selected for this work are summarized in Table 2. In addition, the main fuel properties studied are summarized in Table 3.
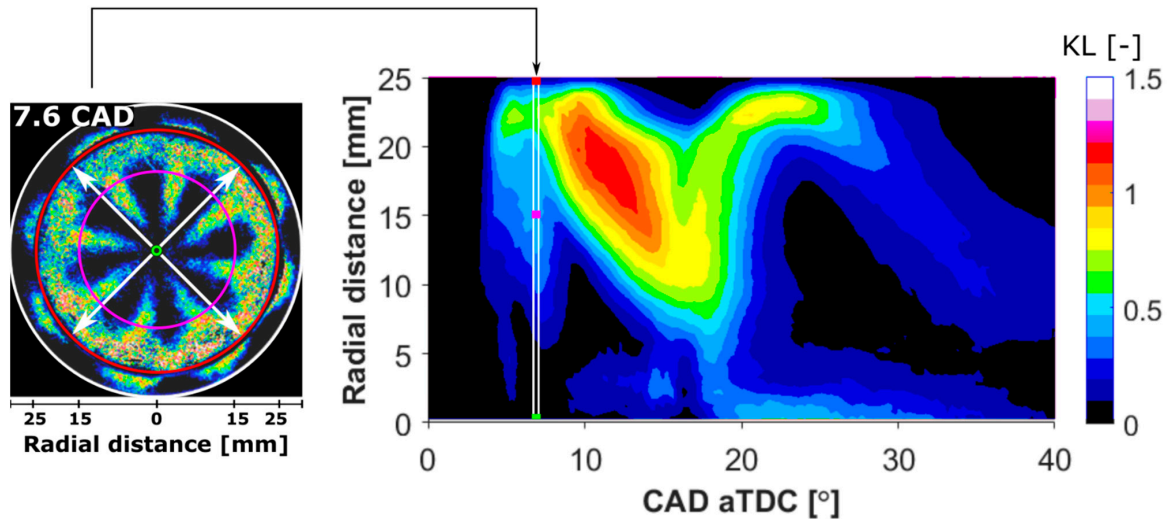

Figure 5. A sketch of the methodology used to represent KL evolution maps.

Table 2. Engine operating conditions.

Operating Conditions	
Piston bowl	Conventional/Radial-lips
Engine speed [rpm]	1400
Injector	CDS
BMEP [bar]	6
Inj. Scheduling & Rail Pressure	Multiple @ 1182 bar
Intake pressure [bar]	1.34
Exhaust pressure [bar]	1.54

Table 3. Main fuel properties used in this study.

	EN 590 Diesel	OME$_X$
Density [kg/m^3] (T = 15 °C)	829.20	1057.10
Viscosity [mm^2/s] (T = 40 °C)	2.59	1.08
Lubricity [µm]	386	320
Cetane number [-]	52.0	68.6
Carbon content [% m/m]	86.2	44.2
Hydrogen content [% m/m]	13.8	8.8
Oxygen content [% m/m]	0	45
Lower heating value [MJ/kg]	41.92	19.21

An injection strategy consisting of 2 pilots, 1 main and 1 post-injection, was used. The main injection pulse was adjusted to keep the same energy released between fuels (@21% O$_2$), compensating for the lower OMEx's lower heating value (LHV). This adjustment allows us to keep the same engine load for all cases. The dwell time between the end of the main injection and the start of the post-injection was kept constant by appropriately shifting the last pulse. Figure 6 shows the electric injection signals adopted for each fuel and the duration in µs of the main injection.
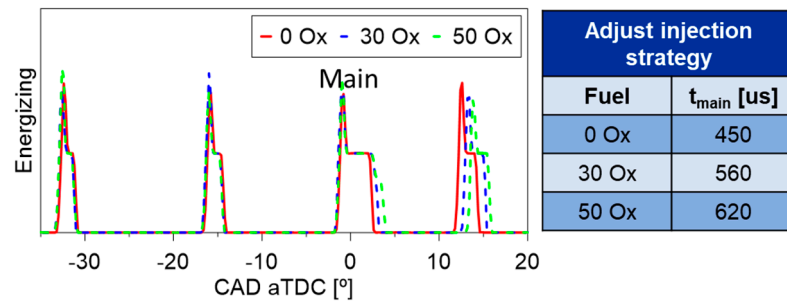
Figure 6. Details on fuel injection strategy.

3. Results and Discussion

3.1. Conventional Piston

As reported in the scientific literature [6], using OME_X improves the reduction of in-cylinder soot formation during the combustion process. Furthermore, the combustion speed event increases, reducing its duration when using this fuel.

The first part of the analysis aims to describe the behavior of the different blends and the benefits of increasing OME_x content with the conventional piston (CP). The upper part of Figure 7 shows the distribution of KL values at different CADs for three different OME_X percentages in the fuel: 0 Ox (top), 30 Ox (middle), and 50 Ox (bottom), at 21% O_2 to illustrate the temporal evolution during the combustion process inside the combustion chamber. The bottom part of the figure shows the apparent rate of heat release (aRoHR) profiles and the average KL curves for the selected fuels from the top dead center (TDC) to 28 CAD aTDC. As color rectangles, the aRoHR plots highlight the duration of the main and post injections (retrieved from high-speed images).
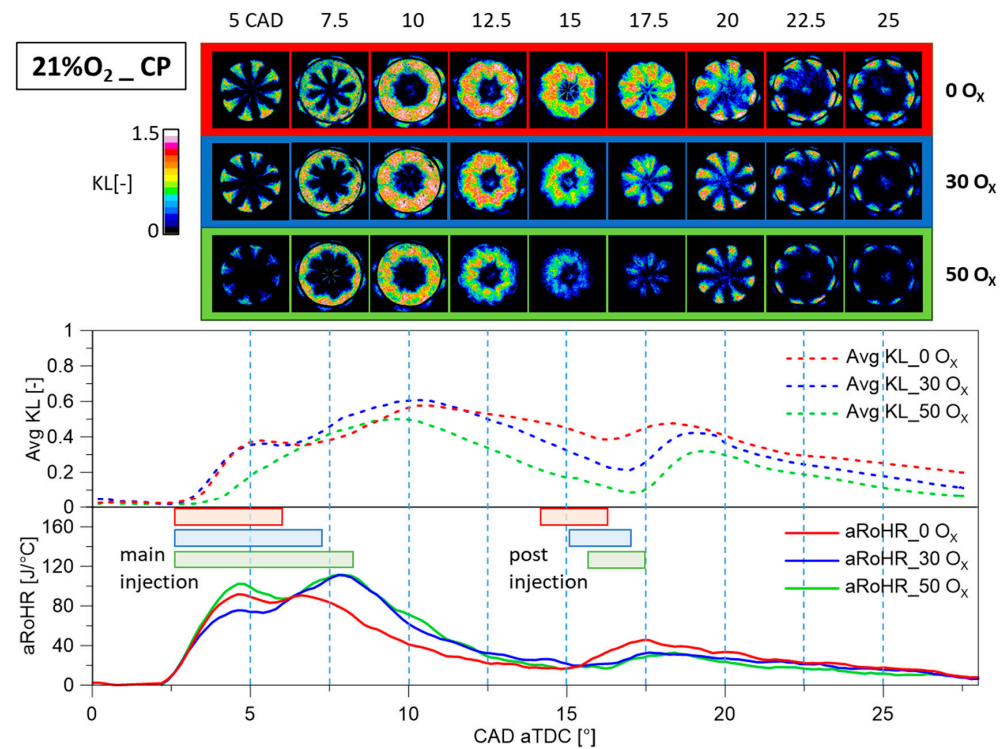

Figure 7. KL factor imaging evolution, average KL, and aRoHR for 0 Ox, 30 Ox, and 50 Ox at 21% O_2. The results correspond to the average of 10 combustion cycles.

The main injection starts at ~2.5 CAD aTDC, and, as stated previously, its duration depends on the OME_X percentage in the blend. During the main injection (frame@5 CAD), producing soot allows for identifying a diffusive flame's characteristic structure. A few

CADs later, the sprays impinge on the piston bowl wall, and the burning jets expand tangentially, interacting between them and merging, forming a crown. For 50 Ox, the liquid fuel sprays are still visible around the nozzle at 7.5 CAD aTDC because of the longer injection duration compared to 0 Ox and 30 Ox. For all mixtures, at this stage, the soot production is more relevant than the oxidation process (increase in area and intensity) until around 10 CAD aTDC. After this instant, the reduction in intensity and area of the KL distribution indicates that the soot oxidation processes dominate overproduction.

The peak of aRoHR corresponding to the main injection shows clearer staged combustion when increasing the OME_x percentage in the blend. The first stage, which corresponds to the first peak, is related to the premixed combustion phase. The second stage, which corresponds to the diffusive combustion stage, is more intense for 30 Ox and 50 Ox due to the longer duration of the main injection when increasing OME_x content. When the post-injection starts, the KL curve for 30 Ox and 50 Ox suggests that a big part of the soot produced has already been oxidized. Therefore, the expected benefits of post-injection (increasing late oxidation) are not so evident.

In contrast, a significant increase of soot is observed. However, with Diesel, the KL curve suggests higher soot levels at this stage. In this scenario, the contribution of pilot injection has more potential to improve oxidation, and it causes a minor increase in the KL curve. However, the soot remaining from the combustion of the main injection is added to the soot produced during the combustion of the post-injection, resulting in soot levels higher than for the other blends. The fact that the post-injection peak of aRoHR is reduced when increasing OME_x percentage in the blend indicates that the oxygenated fuel allowed a complete main injection combustion resulting in less fuel partially or not oxidized.

With all discussed above, a clear in-cylinder soot reduction and faster combustion event are reported when increasing the quantity of OME_X in the fuel, consistent with what can be found in the literature. Thanks to this, OME_X seems promising to maintain low levels of soot formation when applying other strategies to reduce the temperature chamber (like EGR), to reduce the NO_X formation. This strategy increases the soot formation due to the reduction of fresh oxygen inside the cylinder, leading to the well-known trade-off between soot and NO_X.

To evaluate this, EGR was simulated by reducing the oxygen concentration at the intake by up to 15%. A comparison of KL distribution inside the combustion chamber, the KL evolution curves, and the aRoHR for 50 Ox at 21% O_2 and 15% O_2 are shown in Figure 8. At the first CAD represented in this figure, for 15% O_2, no KL values can be observed due to the later start of combustion typical of EGR conditions. This is consistent with the aRoHR shown. Until approximately 10 CAD, lower KL values and a smaller area can be observed for 15% compared to 21% O_2. After that, the trend is reversed. When the post-injection occurs (~15 CAD), the 21% O_2 case shows much lower KL values than the 15% O_2 case. This highlights the difficulty of this operating condition to oxidize soot. Besides, it confirms the importance of ambient oxygen for oxidation and the reduction of soot levels inside the cylinder, even using 50% OME_X in the fuel.

The reduction of oxygen concentration has a similar effect over all the fuels considered in this study. In summary, the KL evolution curves for all fuels are reported in Figure 9 for 21% and 15% O_2. The curves show that even 50 Ox at 15% O_2 forms more soot than any other blends at 21% O_2.

The results show that the O_2 contained in the molecule of OME_X is insufficient at high EGR conditions to keep the same soot levels as without EGR. Using neat OME_X would indeed be able to improve the soot reduction further. However, the incompatibility with elements of the injection system and the increased fuel injected to achieve the same energy released by the fuel make that not a good option to consider. For these reasons, it is necessary to implement additional strategies to improve soot reduction without increasing OME_X content in the fuel.
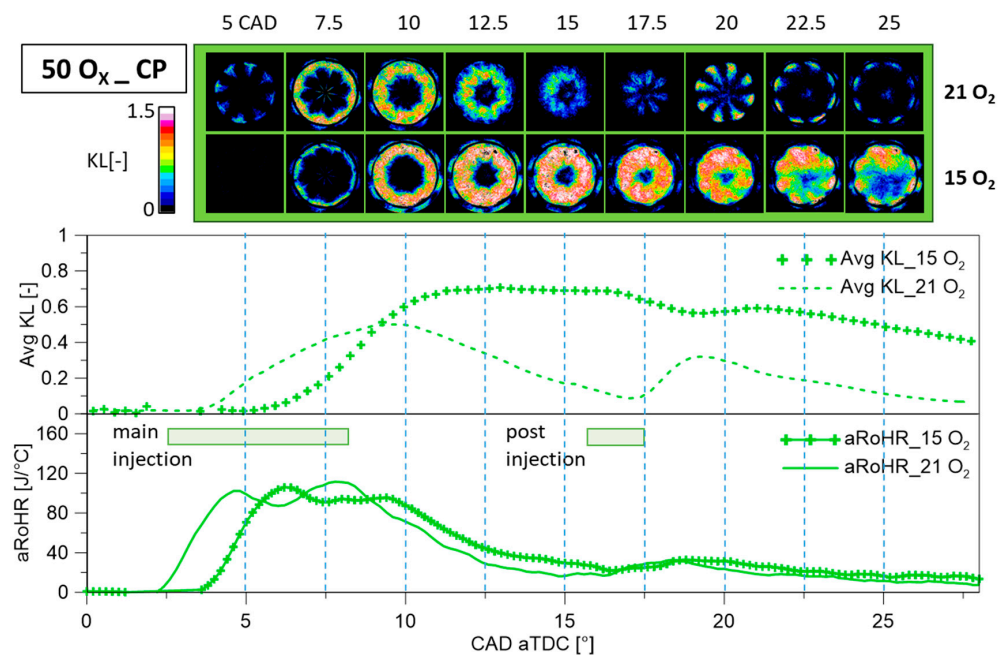
Figure 8. KL factor imaging evolution, KL evolution curves, and aRoHR for 50% Ox in fuel at 21% O_2 and 15% O_2. The results correspond to the average of 10 combustion cycles.
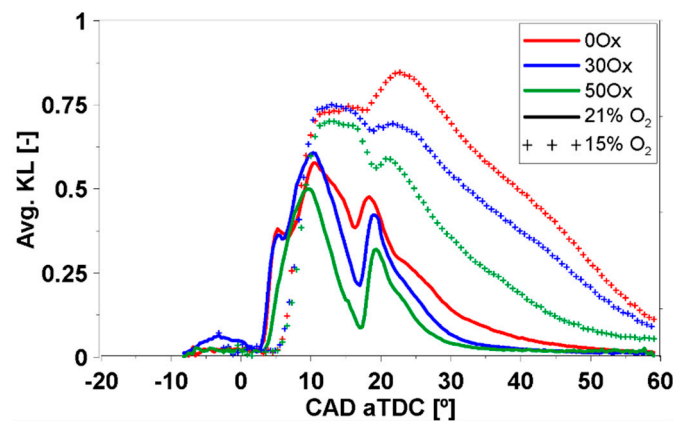

Figure 9. KL evolution curves using 0 Ox, 30 Ox, and 50 Ox in the fuel at 21% O_2 and 15% O_2.

3.2. Radial-Lips Piston

As previously discussed, this study tested a second bowl geometry (RP) containing a stepped lip at the bowl edge and radial lips.

KL distribution and the KL/OH* radial maps are presented in Figures 10 and 11, respectively, to show the temporal and spatial evolution for both pistons using 50 Ox at 15% O_2. The first thing that can be observed is a different aRoHR evolution. The RP piston provides a faster ignition and a much more intense heat release than the CP. This is relevant as it compensates for the delay caused by the oxygen reduction that was previously mentioned. Regarding soot production, higher KL values are reported for the conventional piston during the whole combustion event. The first KL values appear close to the bowl periphery at 7.5 CAD, probably due to the flame-to-flame interaction after impacting the bowl wall, as seen in Figure 12. After this, the high KL cloud evolves toward the center of the bowl until 20 CAD (before the post-injection combustion). The movement of the KL cloud and OH* reactions can be seen clearly in radial maps (left images from Figure 11). During the same interval, the low values of OH* in the radial map confirm that the soot is hardly oxidized, resulting in the high KL cloud mentioned previously. The lack of

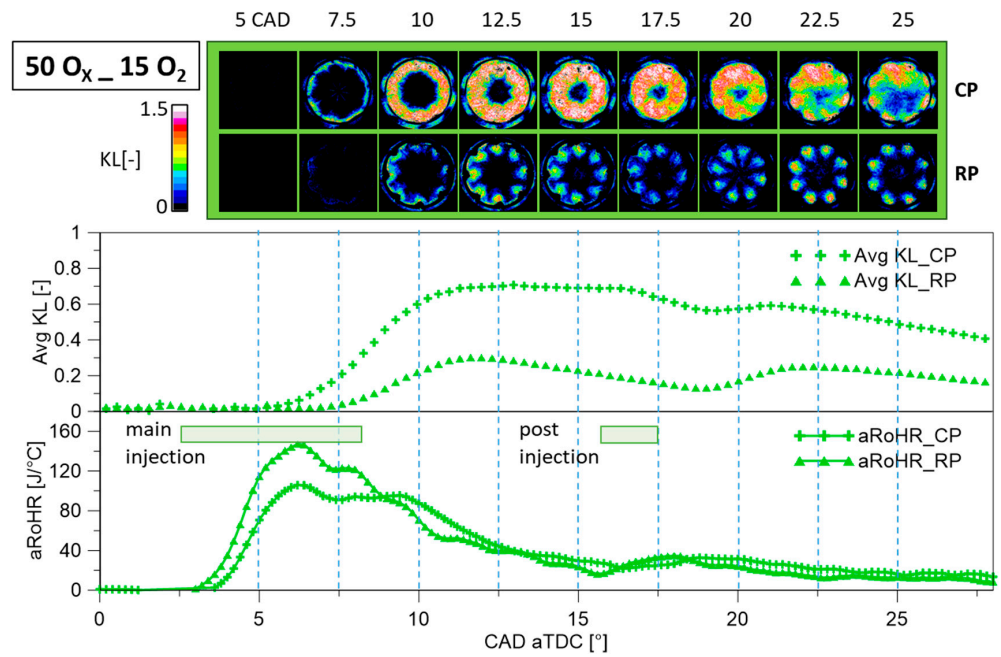oxygen available due to its low concentration difficulties the soot cloud oxidation, even for this blend.

Figure 10. KL factor imaging evolution, KL evolution curves, and aRoHR for 50 Ox at 15% O_2 using conventional (CP) and radial (RP). The results correspond to the average of 10 combustion cycles.
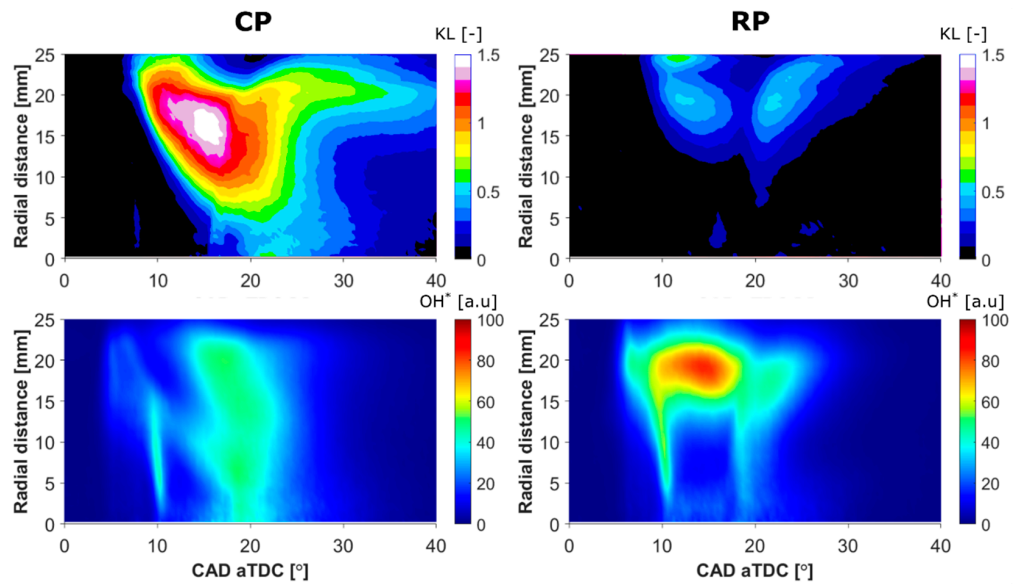

Figure 11. KL (**top**) and OH* (**bottom**) radial maps using conventional (**left**) and radial (**right**) pistons at 50 Ox and 15% O_2.
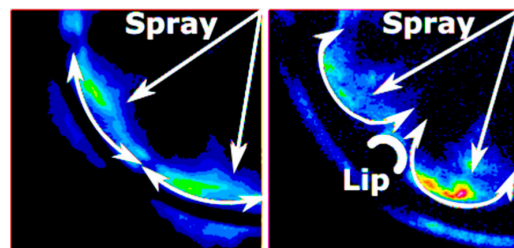

Figure 12. Flame distribution due to conventional (**left**) and radial-lips (**right**) pistons.

In contrast, the RP piston shows several differences, which lead to lower KL values. The first KL values also appear at the bowl periphery and evolve toward the center of the bowl, as in the conventional piston case. However, the intensity of KL values is significantly lower for this piston, and the OH* radial map (see the right image from Figure 11) confirms a higher oxidation activity from the periphery to a 15 mm radius during the main injection combustion event. This suggests that less soot is formed but is also significantly oxidized before the beginning of the post-injection combustion event, as seen in Figure 10 at 17.5 CAD. This fact is also visible in the KL radial map of Figure 11. Here, two different KL clouds separated by a dark gap around 20 CAD can be observed, indicating that the oxidation process during the main injection combustion event is sufficient to oxidize a big part of the soot formed. The results report an improvement in oxidizing the in-cylinder soot formation using radial lip geometry with low oxygen concentration inside the combustion chamber compared to the conventional piston.

From the sequence of images shown in Figure 10, it is possible to see that, in contrast with CP, the RP geometry reduces the interaction between flames at the periphery of the bowl. As shown in Figure 12, the presence of radial lips prevents the flames from spreading tangentially, creating a backward movement instead. This reduces the flame-to-flame interaction, reducing the formation of high equivalence ratio regions and promoting the use of fresh oxygen close to the center of the bowl [24]. In addition, the stepped lip improves the oxidation of part of the fuel at the squish region compared to the CP geometry.

To summarize the performance of the RP in combination with the fuel, KL evolution curves for all fuels tested in this study at two oxygen concentrations (21% and 15%) are reported in Figure 13. The results show the same behavior discussed previously for all the cases. The RP reduces soot formation and improves its oxidation during combustion, independently of the oxygen concentration. However, its effect is more prominent at 15% O_2. This indicates that RP is more effective than CP under low oxygen concentrations. To quantify the reduction in terms of KL achieved with RP for each fuel, the relative reduction of KL values at 15% O_2 has been calculated according to Equation (1):

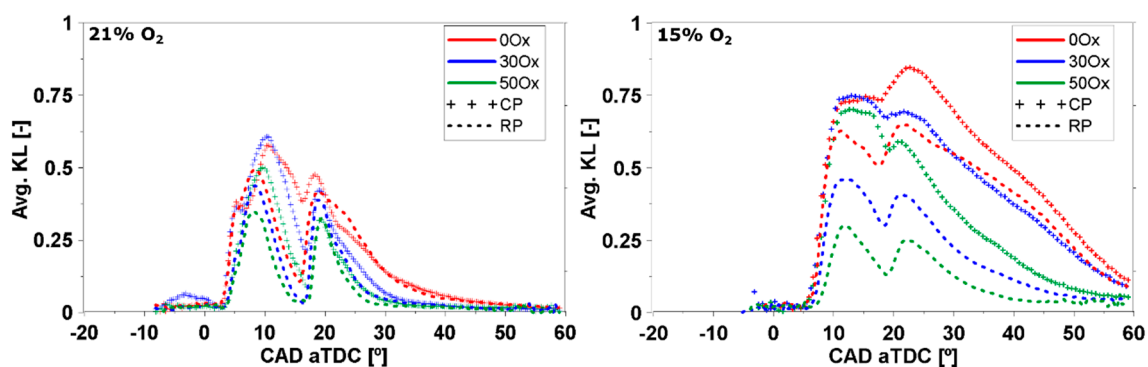$$Rel.\ KL = \frac{Avg.KL_{CP} - Avg.KL_{RP}}{Avg.KL_{CP}} \tag{1}$$

Figure 13. KL evolution curves using 0 Ox, 30 Ox, and 50 Ox in the fuel at 21% O_2 (**left**) and 15% O_2 (**right**) for conventional and radial-lips pistons.

The Rel. KL evolution for the three fuels considered in this study is shown in Figure 14. Between 0 and 20 CAD aTDC, the KL reduction achieved with the RP with 0 Ox varies from 10% to 45%. In the same interval, a much higher reduction is achieved when increased the OME_X content in the blend. For 30 Ox, it varies between 40% and 75%, while for 50 Ox, it reaches from 30% to 80%, depending on the combustion stage. During the late stages of combustion, the KL reduction using the RP is 17%, 70%, and 70% for 0 Ox, 30 Ox, and 50 Ox, respectively. Therefore, the trend shows a clear improvement in soot reduction when combining the radial-lips design with OME_X content in the fuel, especially at low ambient oxygen concentrations, which are representative of low NO_X operating conditions. When

comparing 21% and 15% O_2, it is possible to see that the RP can keep the same KL values with 30 Ox and 50 Ox. The level reached with both oxygen concentrations is similar when looking at the two peaks. However, when looking at the interval between peaks and the late oxidation stage, it is possible to see that KL decreases much faster with 21% O_2. This behavior suggests that the oxygen in the fuel strongly impacts the soot formation (and the maximum KL reached) with RP. In contrast, the ambient oxygen controls the oxidation (and the velocity with which the KL decreases). However, this is not observable with 0 Ox.
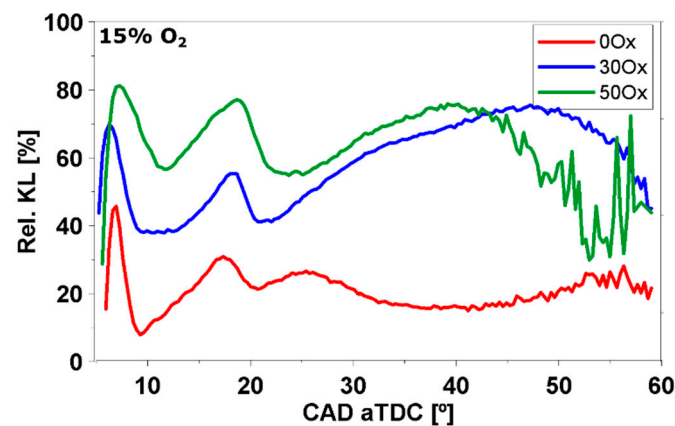

Figure 14. KL values reduction percentage using radial-lips piston compared to conventional piston for all fuels at 15% O_2.

To summarize the differences between piston geometries and all fuels tested, the area below the KL evolution curves from Figure 13 is plotted in Figure 15. The aim is to represent the accumulation of KL reached along the combustion process. The curves corresponding to CP at 21% O_2 for all fuels are plotted with solid lines for reference. The 15% O_2 cases show a higher accumulation of KL when using CP compared to the RP one. The use of this piston achieves a reduction of 37%, 70%, and 78% using 0%, 30%, and 50% of OME_x in the fuel, respectively. It is true that without OME_X in the fuel (0 Ox), the CP (red-solid line) reaches a 48% lower value for 21% O_2 than RP at the lowest oxygen concentration condition using the same fuel (red-dashed line). However, when combined with OME_X in the blend, the RP achieves similar values as the cases using the CP at 21% O_2. Even with 50 Ox, the values reported are below the ones corresponding to the reference case. On the one hand, this indicates that using only the piston geometry with low oxygen concentration inside the combustion chamber is insufficient to achieve or improve the soot levels significantly compared to using a CP geometry with no EGR. On the other hand, it confirms a synergy when combining oxygenated fuels (blended with Diesel) with the RP geometry, as the effect of reducing ambient oxygen concentration over soot is almost negligible.
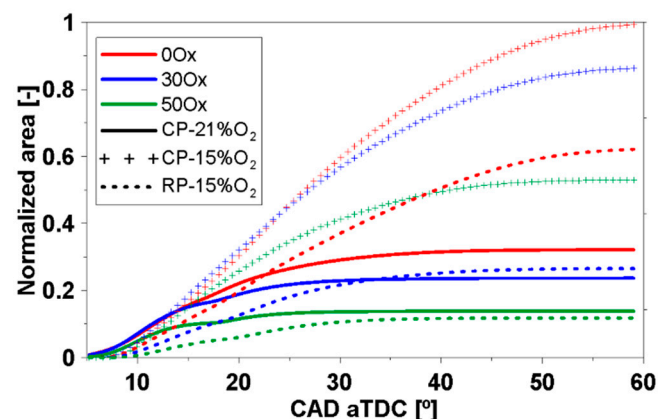

Figure 15. Normalized average KL closed curves area.

4. Summary and Conclusions

The main results of this study are summarized below in bullet points.

Regarding the conventional piston:

- At no-EGR condition (21% O_2), the reduction of KL is more prominent when increasing the OME_X quantity in the blend, which agrees with what can be found in the literature.
- The OME_X content in the blend reduces the amount of soot formed, even at 15% O_2. However, results confirm that only OME_X (up to 50%) is insufficient to avoid the increase because of the reduction of ambient oxygen.

Regarding the radial-lips piston:

- The avoidance of flame-to-flame interaction achieved by the radial-lips feature results in lower soot formation close to the bowl wall. In addition, the redirection of flames toward the center of the piston takes advantage of the oxygen available and significantly improves soot oxidation.
- The addition of OME_X improves the radial-lips piston geometry benefits. In the most unfavorable condition (15% O_2), the addition of OME_X can extend the KL reduction achieved by the novel piston geometry from 17% (0 Ox) up to 70% (50 Ox) during the late stage of combustion.
- Results show that 30% and 50% OME_X in the blend, in combination with the radial-lips piston, can provide similar soot levels with 15% and 21% O_2. This confirms the potential of this combined solution to reduce soot levels when using EGR significantly.

The reported synergy between OME_X and the radial-lips concept represents a promising solution to mitigate the existing soot-NO_X trade-off-. It opens a path to using temperature reduction strategies like EGR to minimize NO_X formation without compromising soot emissions.

This study has analyzed the potential of different OME_X-Diesel blends (0%, 30%, and 50%) in combination with a novel radial-lips piston geometry under high EGR rate condition (15% O_2). However, this work presents some limitations that future works should overcome. As previously mentioned, only the duration of the main injection was modified to compensate for the lower LHV of OME_X to reach the same engine load for all cases. Future studies should explore further improvement and optimization of the injection strategy for the blends by modifying other parameters, such as the number of injections, the injection pressure, or the delay between pulses. In addition, the study analyzed the combustion behavior in an optical engine, which has certain limitations in terms of operating conditions compared to more conventional engines. Therefore, to extend the application of the results presented here, a similar study in a full-metal version of a single-cylinder engine would be beneficial to analyze the exhaust emissions and corroborate what has been observed inside the cylinder and has been reported in this work.

Abbreviations

EU	European Union.
GHG	Greenhouse gas.
ICE	Internal combustion engine.
CI	Compression ignition.
SI	Spark ignition.
FCVs	Fuel cell vehicles.
WTW	Well-to-wheels.
OME_n	Oxymethylene dimethyl ether
CDS	Controlled diffusive spray.
UV	Ultraviolet.
CMOS	Complementary metal oxide semiconductor.
OH*	Excited state hydroxyl radical.
2C	2-Color pyrometry.
CP	Conventional piston.
RP	Radial-lips piston.
CAD	Crank angle degree.
aRoHR	The apparent rate of heat release.
BMEP	Break mean effective pressure.
T_{int}	Intake temperature.
P_{inj}	Injection pressure.
P_{int}	Intake pressure.
P_{exh}	Exhaust pressure.
SOE	Start of energizing.
$\% O_2$	Oxygen concentration (volume)
EGR	Exhaust gas recirculation.
FWHM	Full width half maximum.
KL	Soot optical thickness.
LHV	Lower heating value.
aTDC	After the top dead center.

References

1. Air Pollution—European Environment Agency n.d. Available online: https://www.eea.europa.eu/themes/air (accessed on 13 December 2022).
2. Al Ezzi, A.; Fayad, M.A.; Al Jubori, A.M.; Jaber, A.A.; Alsadawi, L.A.; Dhahad, H.A.; Chaichan, M.T.; Yusaf, T. Influence of fuel injection pressure and RME on combustion, NO emissions and soot nanoparticles characteristics in common-rail HSDI diesel engine. *Int. J. Thermofluids* **2022**, *15*, 100173. [CrossRef]
3. Rajak, U.; Nashine, P.; Verma, T.N. Performance analysis and exhaust emissions of aegle methyl ester operated compression ignition engine. *Therm. Sci. Eng. Prog.* **2019**, *12*, 100354. [CrossRef]
4. Chaurasiya, P.K.; Rajak, U.; Veza, I.; Verma, T.N.; Ağbulut, Ü. Influence of injection timing on performance, combustion and emission characteristics of a diesel engine running on hydrogen-diethyl ether, n-butanol and biodiesel blends. *Int. J. Hydrogen Energy* **2022**, *47*, 18182–18193. [CrossRef]
5. Liu, H.; Wang, Z.; Li, Y.; Zheng, Y.; He, T.; Wang, J. Recent progress in the application in compression ignition engines and the synthesis technologies of polyoxymethylene dimethyl ethers. *Appl. Energy* **2019**, *233–234*, 599–611. [CrossRef]
6. Chen, H.; Su, X.; He, J.; Zhang, P.; Xu, H.; Zhou, C. Investigation on combustion characteristics of cyclopentanol/diesel fuel blends in an optical engine. *Renew. Energy* **2021**, *167*, 811–829. [CrossRef]
7. Pöllmann, S.; Härtl, M.; Jaensch, M.; Wachtmeister, G. Evaluation of strategies to optimize engine efficiency and NOx emissions with the synthetic diesel fuel oxymethylene ether. *Int. J. Engine Res.* **2023**, 146808742211448. [CrossRef]
8. Benajes, J.; García, A.; Monsalve-Serrano, J.; Sari, R. Clean and efficient dual-fuel combustion using OMEx as high reactivity fuel: Comparison to diesel-gasoline calibration. *Energy Convers. Manag.* **2020**, *216*, 112953. [CrossRef]
9. Xu, Z.; Duan, X.; Liu, Y.; Deng, B.; Liu, J. Spray combustion and soot formation characteristics of the acetone-butanol-ethanol/diesel blends under diesel engine-relevant conditions. *Fuel* **2020**, *280*, 118483. [CrossRef]
10. Chen, Y.; Liu, S.; Guo, X.; Jia, C.; Huang, X.; Wang, Y.; Huang, H. Experimental Research on the Macroscopic and Microscopic Spray Characteristics of Diesel-PODE$_{3-4}$ Blends. *Energies* **2021**, *14*, 5559. [CrossRef]
11. Lin, Q.; Tay, K.L.; Zhao, F.; Yang, W. Enabling robust simulation of polyoxymethylene dimethyl ether 3 (PODE$_3$) combustion in engines. *Int. J. Engine Res.* **2022**, *2022*, 1522–1542. [CrossRef]

12. Benajes, J.; Garcia-Oliver, J.M.; Pastor, J.M.; De Leon-Ceriani, D. Unsteady Flamelet modeling study on OMEx-type fuels under Engine Combustion Network Spray A conditions. *Fuel* **2023**, *331*, 125458. [CrossRef]

13. Pastor, J.V.; García, A.; Micó, C.; Lewiski, F. Simultaneous high-speed spectroscopy and 2-color pyrometry analysis in an optical compression ignition engine fueled with OME$_X$-diesel blends. *Combust. Flame* **2021**, *230*, 111437. [CrossRef]

14. Liu, J.; Wang, L.; Wang, P.; Sun, P.; Liu, H.; Meng, Z.; Zhang, L.; Ma, H. An overview of polyoxymethylene dimethyl ethers as alternative fuel for compression ignition engines. *Fuel* **2022**, *318*, 123582. [CrossRef]

15. He, J.; Chen, H.; Su, X.; Xie, B.; Li, Q. Combustion Study of Polyoxymethylene Dimethyl Ethers and Diesel Blend Fuels on an Optical Engine. *Energies* **2021**, *14*, 4608. [CrossRef]

16. García, A.; Gil, A.; Monsalve-Serrano, J.L.; Sari, R.L. OMEx-diesel blends as high reactivity fuel for ultra-low NOx and soot emissions in the dual-mode dual-fuel combustion strategy. *Fuel* **2020**, *275*, 117898. [CrossRef]

17. Martins, J.; Brito, F.P. Alternative Fuels for Internal Combustion Engines. *Energies* **2020**, *13*, 4086. [CrossRef]

18. Wei, Y.; Zhang, Y.; Zhu, Z.; Zhu, X.; Gu, H.; Liu, S. Effect of PODE on Emission Characteristics of a China VI Heavy-Duty Diesel Engine. *Appl. Sci.* **2022**, *12*, 1108. [CrossRef]

19. Tornatore, C.; Bozza, F.; De Bellis, V.; Teodosio, L.; Valentino, G.; Marchitto, L. Experimental and numerical study on the influence of cooled EGR on knock tendency, performance and emissions of a downsized spark-ignition engine. *Energy* **2019**, *172*, 968–976. [CrossRef]

20. Wei, Y.; Zhang, C.; Zhu, Z.; Zhang, Y.; He, D.; Liu, S. Numerical Optimization of the EGR Rate and Injection Timing with a Novel Cavitation Model in a Diesel Engine Fueled with PODE/Diesel Blends. *Appl. Sci.* **2022**, *12*, 12556. [CrossRef]

21. Kakaee, A.-H.; Nasiri-Toosi, A.; Partovi, B.; Paykani, A. Effects of piston bowl geometry on combustion and emissions characteristics of a natural gas/diesel RCCI engine. *Appl. Therm. Eng.* **2016**, *102*, 1462–1472. [CrossRef]

22. Temizer, I.; Cihan, O. Effect of piston geometry on combustion characteristics of CI engine used Sal seed oil. *Int. J. Engine Res.* **2022**, 146808742211434. [CrossRef]

23. Pham, V.C.; Kim, J.K.; Lee, W.-J.; Choe, S.-J.; Le, V.V.; Choi, J.-H. Effects of Piston Bowl Geometry on Combustion and Emissions of a Four-Stroke Heavy-Duty Diesel Marine Engine. *Appl. Sci.* **2022**, *12*, 13012. [CrossRef]

24. Pastor, J.V.; Micó, C.; Lewiski, F.; Tejada, F.J.; Vassallo, A. Innovative diesel piston geometries for soot emissions reduction and cleaner combustion: An optical investigation. In Proceedings of the Thiesel 2022 Conference on Thermo- and Fluid Dynamics of Clean Propulsion Powerplants, Valencia, Spain, 13–16 September 2022.

25. Eismark, J.; Andersson, M.; Christensen, M.; Karlsson, A.; Denbratt, I. Role of Piston Bowl Shape to Enhance Late-Cycle Soot Oxidation in Low-Swirl Diesel Combustion. *SAE Int. J. Engines* **2019**, *12*, 233–249. [CrossRef]

26. Smith, A. *Ricardo Low Emissions Combustion Technology Helps JCB Create the Off-Highway Industry's Cleanest Engine*; Ricardo Press: Shoreham-by-Sea, UK, 2010; pp. 4–6.

27. Neely, G.D.; Sasaki, S.; Sono, H. *Investigation of Alternative Combustion Crossing Stoichiometric Air Fuel Ratio for Clean Diesels*; SAE Technical Papers; SAE International: Warrendale, PA, USA, 2007. [CrossRef]

28. Di Blasio, G.; Ianniello, R.; Beatrice, C.; Pesce, F.C.; Vassallo, A.; Belgiorno, G. Experimental Investigation on an Innovative Additive Manufacturing-Enabled Diesel Piston Design to improve Engine-out Emissions and Thermal Efficiency beyond Euro6. In Proceedings of the THIESEL 2020 Conference on Thermo- and Fluid Dynamic Processes in Direct Injection Engines, Valencia, Spain, 8–11 September 2020.

29. Di Blasio, G.; Ianniello, R.; Beatrice, C.; Pesce, F.C.; Vassallo, A.; Belgiorno, G. Additive manufacturing new piston design and injection strategies for highly efficient and ultra-low emissions combustion in view of 2030 targets. *Fuel* **2023**, *346*, 128270. [CrossRef]

30. Serizawa, K.; Ueda, D.; Mikami, N.; Tomida, Y.; Weber, J. *Realizing Robust Combustion with High Response Diesel Injector with Controlled Diffusive Spray Nozzle and Closed Loop Injection Control*; SAE Technical Papers; SAE International: Warrendale, PA, USA, 2017. [CrossRef]

31. Tu, P.-W.; Xu, H.; Srivastava, D.K.; Dean, K.; Jing, D.; Cao, L.; Weall, A.; Venus, J.K. *Numerical Investigation of GDI Injector Nozzle Geometry on Spray Characteristics*; SAE Technical Papers; SAE International: Warrendale, PA, USA, 2015. [CrossRef]

32. Payri, R.; De La Morena, J.; Monsalve-Serrano, J.; Pesce, F.C.; Vassallo, A. Impact of counter-bore nozzle on the combustion process and exhaust emissions for light-duty diesel engine application. *Int. J. Engine Res.* **2018**, *20*, 46–57. [CrossRef]

33. Payri, R.; Hardy, G.; Gimeno, J.; Bautista, A. Analysis of counterbore effect in five diesel common rail injectors. *Exp. Therm. Fluid Sci.* **2019**, *107*, 69–78. [CrossRef]

34. Pastor, J.V.; Olmeda, P.; Martín, J.; Lewiski, F. Methodology for Optical Engine Characterization by Means of the Combination of Experimental and Modeling Techniques. *Appl. Sci.* **2018**, *8*, 2571. [CrossRef]

35. Higgins, B.; Siebers, D.L. *Measurement of the Flame Lift-Off Location on DI Diesel Sprays Using OH Chemiluminescence*; SAE Technical Papers; SAE International: Warrendale, PA, USA, 2001. [CrossRef]

36. Dec, J.E.; Coy, E.B. *OH Radical Imaging in a DI Diesel Engine and the Structure of the Early Diffusion Flame*; SAE Technical Papers; SAE International: Warrendale, PA, USA, 1996. [CrossRef]

37. Zhao, H. *Laser Diagnostics and Optical Measurement Techniques in Internal Combustion Engines*; SAE International: Warrendale, PA, USA, 2012. [CrossRef]

38. Lowe, D.G. Distinctive Image Features from Scale-Invariant Keypoints. *Int. J. Comput. Vis.* **2004**, *60*, 91–110. [CrossRef]